Journal of
Applied Crystallography
ISSN 0021-8898
Editor: **Anke R. Kaysser-Pyzalla**

Coating thickness determination in highly absorbent core–shell systems

Herve Palancher, Anne Bonnin, Veijo Honkimäki, Heikki Suhonen, Peter Cloetens, Tobias Zweifel, Rémi Tucoulou, Alexander Rack and Marco Voltolini

J. Appl. Cryst. (2012). **45**, 906–913

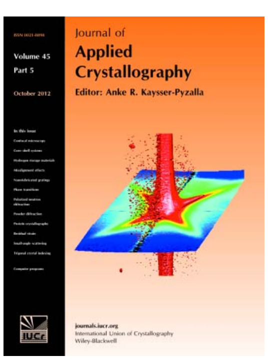

Journal of
Applied Crystallography
ISSN 0021-8898

Received 27 March 2012
Accepted 9 July 2012

Coating thickness determination in highly absorbent core–shell systems

Herve Palancher,[a]* Anne Bonnin,[a,b] Veijo Honkimäki,[b] Heikki Suhonen,[b] Peter Cloetens,[b] Tobias Zweifel,[a,c] Rémi Tucoulou,[b] Alexander Rack[b] and Marco Voltolini[b,d]

[a]CEA, DEN, DEC, F-13108 St Paul Lez Durance Cedex, France, [b]ESRF, 6 rue J. Horowitz, 38000 Grenoble Cedex, France, [c]Forschungsneutronenquelle Heinz Maier-Leibnitz (FRM II), Technische Universität München, D-85747 Garching bei München, Germany, and [d]Department of Geoscience, University of Padua, I-35131 Padua, Italy. Correspondence e-mail: herve.palancher@cea.fr

This article describes a single-shot methodology to derive an average coating thickness in multi-particle core–shell systems exhibiting high X-ray absorption. Powder composed of U–Mo alloy particles surrounded by a micrometre-thick UO_2 protective layer has been used as a test sample. Combining high-energy X-ray diffraction and laser granulometry, the average shell thickness could be accurately characterized. These results have been validated by additional measurements on single particles by two techniques: X-ray nanotomography and high-energy X-ray diffraction. The presented single-shot approach gives rise to many potential applications on core–shell systems and in particular on as-fabricated heterogeneous nuclear fuels.

1. Introduction

Within the framework of the RERTR program (Reduced Enrichment for Research and Test Reactors), a new low-enriched ($^{235}U < 20$ wt%) nuclear fuel is under development for research reactors. The current most promising concept is based on a dispersion of spherical U–xMo particles (with diameter usually ranging from about 15 up to 125 µm) inside an Al matrix (x denotes the Mo weight fraction in U–xMo alloys; for example, 7 wt% corresponds to about 15.7 at.%). However an intermetallic UMoAl interdiffusion layer (IL) builds up under in-reactor irradiation (Leenaers *et al.*, 2004). This IL is known to exhibit unfavourable properties (bad fission product retention, supposed low thermal conductivity and low density). Therefore, technological studies with the aim of suppressing or limiting its growth are being intensively undertaken worldwide.

The most advanced solutions are generally based on coatings (ZrN, Si *etc.*) of the U–Mo particles: processes using physical or chemical vapour deposition (Van den Berghe *et al.*, 2010), as well as solid–solid reactions (Ryu *et al.*, 2011), have been developed to achieve this goal. A less expensive method involves doping the Al matrix with elements like Si. Such elements diffuse under thermal treatments towards the U–Mo particles and thus form a protective layer around them. Huge interest is currently geared towards the addition of Si to the matrix, since substantial improvements in the in-reactor behaviour have been obtained using this solution (Keiser *et al.*, 2009; Ripert *et al.*, 2011; Charollais *et al.*, 2011). In the case of Si added to the matrix, the protective shell is usually written as SiRDL, standing for Si-rich diffusion layer (the elementary composition of such a layer is complex, comprising the four elements U, Mo, Al and Si). Its thickness is usually small (*i.e.* in the micrometre range) and extremely irregular (i) around a given particle and (ii) from one particle to another (Iltis *et al.*, 2010; Keiser *et al.*, 2011). To further develop this solution (*i.e.* Si addition to the matrix), the characteristics of the SiRDL (Si atomic fraction, covering rate of U–Mo particles, its thickness) have to be tailored and optimized. In this framework, the development of a methodology to determine accurately the average SiRDL thickness is required.

With this view, the use of classical X-ray and electron-based techniques would have been legitimate but appears to be challenging. Because of the large size of the U–xMo core compared to the coating thickness and because of the high X-ray absorption of the γ-U–xMo phase forming the core, full-field micro-computed tomography (CT) and X-ray diffraction (XRD) with a photon energy below 20 keV do not provide reliable results (Bonnin *et al.*, 2011). For scanning electron microscopy (SEM) characterization, the difficulties are linked to the sample preparation, which usually consists of metallographic preparations of these powders: only two-dimensional sections of these particles can be observed and therefore only an apparent thickness can be measured. Indeed particles are seldom cut along their equatorial plane. A precise characterization of these thicknesses would require a huge number of high-resolution SEM observations of particle cross sections, knowledge of the powder granulometry and finally the use of models to estimate a real thickness from these apparent values. Note that, even if similar models have already been developed (Coster & Chermant, 1989), this methodology would be excessively time consuming in terms of SEM characterization.

This work will outline how the outer-shell thickness can be determined by using only two measurements on the coated U–Mo powder: high-energy X-ray diffraction (HE-XRD) and laser granulometry. The results given by this macroscopic scale approach are compared with analyses on single particles by means of HE-XRD and nano-CT. This methodological study is performed on U–7Mo particles protected with a micrometre-thick oxide shell. Such protective layers are easily produced and pretty homogeneous in size (around a given particle and from one particle to another).

2. Theoretical

The weight fraction w_l of each phase l, as given for example by a Rietveld analysis, can be converted into volume fractions (X_l):

$$X_l = (w_l/\rho_l)\Big/\sum_k (w_k/\rho_k), \tag{1}$$

where ρ_l is the density of the phase l.

The volume fractions of the core and of the outer shell can be derived from the XRD measurements using the following relations: $V_{\rm Shell} = \sum_j X_j$ and $V_{\rm Core} = \sum_k X_k$, where the summation extends over the crystallographic phases making up the shell and the core for the first and second sum, respectively.

2.1. Single-particle case

In the case of a single spherical particle with diameter D and an outer shell of thickness e, the calculations of both core and shell volumes are straightforward: $V_{\rm Core}^{\rm Particle} = (4/3)\pi(D/2-e)^3$ and $V_{\rm Shell}^{\rm Particle} = (4/3)\pi(D/2)^3 - V_{\rm Core}^{\rm Particle}$.

The thickness of the outer shell can thus be written as follows:

$$e = \left(\frac{3V_{\rm Core}^{\rm Particle}}{4\pi}\right)^{1/3}\left[-1+\left(\frac{V_{\rm Shell}^{\rm Particle}}{V_{\rm Core}^{\rm Particle}}+1\right)^{1/3}\right]. \tag{2}$$

In the following, if $V_{\rm Shell}^{\rm Particle}/V_{\rm Core}^{\rm Particle}$ is measured, $V_{\rm Core}^{\rm Particle}$ has to be determined from the particle diameter D and the unknown shell thickness e. Therefore an iterative method has to be applied to obtain e. The initial value for e in this iterative calculation has been chosen as $e = (D/2)[-1 + (V_{\rm Shell}^{\rm Particle}/V_{\rm Core}^{\rm Particle} + 1)^{1/3}]$. This enables rapid convergence.

In this section, no relation between the particle size and the outer-shell thickness has been postulated: the two characteristics are considered independent.

2.2. Powder case

When many core–shell particles are illuminated by X-rays at the same time, an average shell thickness is more difficult to obtain. The calculation of the volume ratio between the shell and the core in a powder is based on the powder granulometry $f_V(D)$:

$$\frac{V_{\rm Shell}^{\rm Powder}}{V_{\rm Core}^{\rm Powder}+V_{\rm Shell}^{\rm Powder}} = \frac{\int_0^\infty f_V(D)V_{\rm Shell}^{\rm Particle}\,{\rm d}D}{\int_0^\infty f_V(D)V_{\rm Shell}^{\rm Particle}\,{\rm d}D + \int_0^\infty f_V(D)V_{\rm Core}^{\rm Particle}\,{\rm d}D}, \tag{3}$$

where $V_{\rm core}^{\rm Particle}$ and $V_{\rm Shell}^{\rm Particle}$ are the volumes of the core and the shell, respectively, for a single particle with a diameter D.

To simplify calculations, two assumptions have been made: first that the particles are spherical, and second that the shell thickness e does not depend on the particle diameter D, *i.e.* each particle has the same outer-shell thickness. The validity of such assumptions for oxidized U–7Mo particles will be discussed (see §6).

The ratio $V_{\rm Shell}^{\rm Powder}/(V_{\rm Core}^{\rm Powder} + V_{\rm Shell}^{\rm Powder})$ is referred to as $V_{\rm ratio}$ in the following.

Table 1
Average oxide shell thickness measured by HE-XRD and nano-CT on three powder samples and six particles with characterized diameter.

		Average oxide shell thickness (µm)		
		HE-XRD		
Particle	Mean diameter as measured by SEM (µm)	With theoretical ρ	With measured ρ	Nano-CT
Powder_A	–	0.96 (3)	1.02 (3)	–
Powder_B	–	0.97 (2)	1.03 (2)	–
Powder_C	–	0.82 (7)	0.87 (7)	–
Particle_1	38 (2)	0.84 (24)	0.85 (25)	–
Particle_2	57 (2)	0.94 (17)	1.02 (17)	–
Particle_3	75 (2)	0.85 (10)	0.92 (10)	–
Particle_4	84 (3)	0.88 (13)	0.96 (13)	–
Particle_5	20 (1)	–	–	0.79 (7)
Particle_6	24 (1)	–	–	0.84 (7)

3. Experimental

3.1. Sample preparation

The U–7Mo powder was manufactured using an atomization process by the Korean Atomic Energy Research Institute (Park *et al.*, 2010). At AREVA-CERCA (Romans, France), this powder had subsequently undergone an oxidation treatment [annealing under air at low temperature (493 K) (Jarousse *et al.*, 2008)]. A small part of this powder was embedded in a resin to enable metallographic preparation and then microscopy observations. The coating thickness was evaluated as 1.1 (1) µm by SEM (Iltis, 2009) and 1.3–1.4 µm by optical microscopy (Jarousse *et al.*, 2008).

A first batch, referred to hereafter as Powder_A, was sieved, giving two other batches with particles exhibiting a diameter smaller (Powder_B) and larger (Powder_C) than 45 µm. Six particles were then isolated and fixed on top of quartz capillaries and further analysed by SEM (see Fig. 1); a first indication of both the shape and the dimensions of the particles can be obtained. The largest particles, *i.e.* Particle_3 and Particle_4, exhibit an ellipsoid shape (see Fig. 1*b*). In this case, an apparent diameter has been calculated using measurements performed along three perpendicular directions. These values are reported in Table 1.

3.2. Laser granulometry

The granolumetry of the oxidized powder (Powder_A) was measured by standard laser techniques (Iltis, 2009). The obtained size distribution was fitted with a sum of two normal functions (see Fig. 2). The analytical expression of this function, written as $f_V(D)$ in the following, is given by the equation below:

$$f_V(D) = 0.39N(\mu = 40; \sigma = 7.8)(D) + 0.61N(\mu = 54.3; \sigma = 11.1)(D). \quad (4)$$

In this equation, μ and σ, respectively, define the average and the standard deviation of the normal function. As a reminder the expression for the normal function is

$$N(\mu; \sigma) = \frac{1}{\sigma(2\pi)^{1/2}} \exp\left[-\frac{(D-\mu)^2}{2\sigma^2}\right]. \quad (5)$$

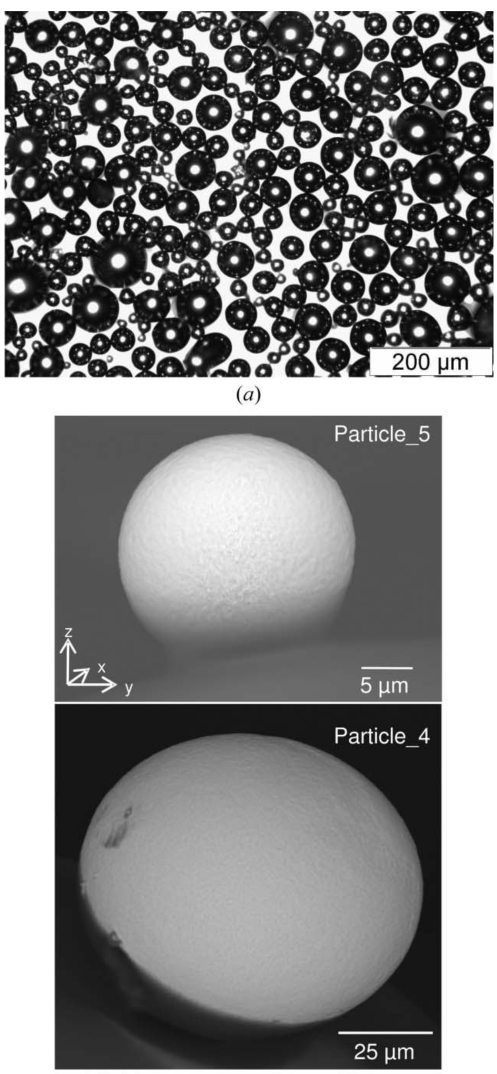

Figure 1
Optical micrograph (*a*) and SEM image (*b*) taken on the oxidized U–7Mo powder and two single particles (Particle_4 and Particle_5), respectively.

3.3. Synchrotron X-ray measurements

Synchrotron X-ray measurements were carried out at the European Synchrotron Radiation Facility (ESRF) in Grenoble (France).

3.3.1. High-energy XRD. Measurements in transmission mode were carried out at the ID15B beamline using a 0.3 × 0.3 mm [vertical (V) × horizontal (H) FWHM] monochromatic X-ray beam.

The oxidized U–7Mo powders were mapped at 87 keV: 60 two-dimensional diffraction patterns were collected on the three samples (Powder_A to Powder_C). For each pattern, the counting time was 40 s. Data were collected using a Pixium flat-panel detector.

For single particles, measurements were slightly adapted: a marCCD detector was preferred to record the data, and particles were submitted to ±50° oscillations so that a maximum of the micrometre-sized U–Mo grains can be put into diffraction conditions (Park *et al.*, 2010). Whereas the three largest particles (referred to as Particle_2 to Particle_4 in Table 1) were analysed with an 87 keV X-ray beam, the smallest (Particle_1) was characterized using a 60 keV beam to optimize the diffracted intensity.

3.3.2. Nano-XRD. Using the sub-micrometre-sized [0.1 × 0.15 μm (V × H FWHM)] X-ray beam available at the nano-imaging station ID22NI (Bleuet *et al.*, 2009; Martínez-Criado, 2012), the crystallographic composition of single oxidized U–Mo particles could be investigated. Measurements were collected at 29 keV using a monochromatic X-ray beam ($\Delta E/E = 1.4 \times 10^{-4}$).

Two kinds of diffraction images were measured: those relating only to the outer oxide shell and those associated with both the U–7Mo core and the oxide shell.

3.3.3. Computed tomography with deep sub-micrometre resolution. Nanotomography measurements were performed on ID22NI on single U–7Mo particles using a 17 keV (just

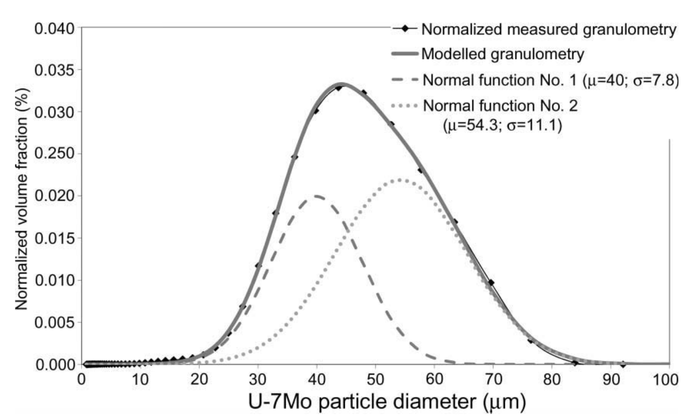

Figure 2
Comparison between measured and calculated granulometries of oxidized U–7Mo powder (Powder_A). The two normal functions used to fit the measured data are also represented.

below the U $L_{\rm III}$-edge) X-ray beam with medium monochromaticity ($\Delta E/E$ = 1.5 × 10^{-2}). It was focused down to approximately 0.09 × 0.13 µm (V × H, FWHM). To preserve the highest spatial resolution and avoid diffraction effects at the sample boundary, a first-generation tomography principle was applied.

The sample was translated horizontally in an on-the-flight acquisition, while the transmitted X-ray intensity was measured in 600 intervals using a silicon drift diode. This linear scan was repeated while the sample was rotated over 180° with 500 steps. This produced a sinogram which was used to reconstruct an image of a single horizontal *xy* slice through the sample. The obtained pixel size in the reconstructed image, *i.e.* the spatial sampling rate, is 0.05 µm. The corresponding high resolution could only be obtained on the smallest particles (Particle_5 and Particle_6); on larger particles, the strong X-ray absorption deteriorates the reconstruction quality.

4. Measurements on single particles

4.1. Crystallographic composition

The measured two-dimensional diffraction patterns were azimuthally integrated using the *Fit2D* software (Hammersley, 1999) and the resulting one-dimensional pattern was refined with the *FullProf* software package based on the Rietveld method (Rodriguez-Carvajal, 1990).

4.1.1. Oxide shell. To investigate the crystallographic composition of the oxide shell, nano-XRD patterns have been measured and then analysed (Palancher *et al.*, 2011). As illustrated by Fig. 3, UO_2 (5.47 Å, *Fm*3*m*) appears to be the only component of this shell. The refinement also shows the presence of less than 0.5 wt% of the cubic γ-U–7Mo phase, which is, however, the main component of the particle core. Two characteristics of the microstructure of this phase may also be seen in this figure. Firstly a strong texture may exist (but is not systematic as deduced from the analysis of other nano-XRD patterns). Secondly UO_2 crystallites are very small in size, probably below the ten nanometre range. Indeed diffraction rings remain continuous despite the very small beam size (see §3.3.2).

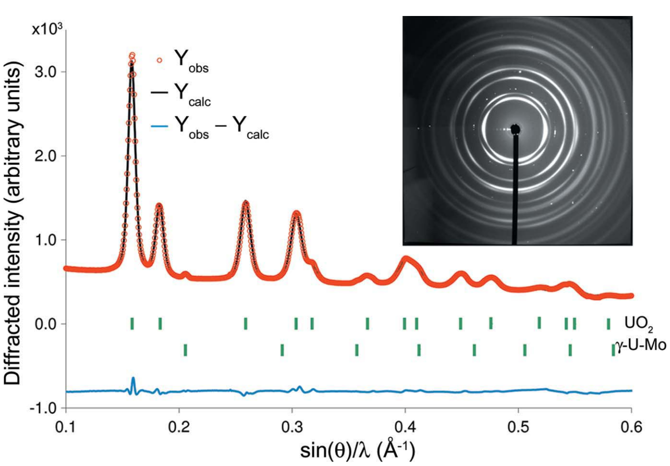

Figure 3
Rietveld analysis of the one-dimensional pattern obtained by nano-XRD at 29 keV on the oxide shell surrounding a U–7Mo core (grey circles; red in the electronic version of the journal). Black and dark-grey (blue in the electronic version) lines indicate the associated calculated and difference patterns, respectively. The inset shows the original two-dimensional diffraction image. The agreement factors for this fit are $R_{\rm p}$ = 5.9%, $R_{\rm wp}$ = 6.2%, χ = 7.5.

When probing the outer part of the shell, a decrease of the lattice parameter (down to 5.44 Å) was noticed, suggesting a slight over-oxidation. This lattice constant decrease is associated with the presence of the cubic β-U_4O_9 (Garrido *et al.*, 2006). Nevertheless these volumes are very limited and the approximation of a single crystallographic component in this oxide shell is fully justified.

Since the Mo solubility in UO_2 is supposed to be lower than 1 at.% (Martin *et al.*, 2003), this fluorite UO_2 phase is very probably locally distorted to accommodate the presence of these large Mo quantities (15 at.%). These defects, however, do not induce long-range distortions that would be identified by our nano-XRD measurements.

4.1.2. Metallic core. High-energy X-ray diffraction on particles is the technique most suited to characterizing the U–7Mo core composition. In the obtained patterns all identified phases except UO_2 (located in the particle outer shell) would belong to the core. As a consequence it can be shown that the core contains only γ-U–*x*Mo, UC (with possibly some O in the structure) and a last trace phase whose structure could not be fully identified (see Appendix *A*). This last phase has not been considered in the quantitative analysis.

The refinement using the Rietveld method has shown that two γ-U–*x*Mo phases with different lattice constants (and thus different Mo content) have to be used to simulate the measured Bragg line asymmetry for this phase (Park *et al.*, 2010).

Table 2 gathers the obtained weight fractions for each phase in each of the four analysed particle samples and Table 3 the agreement factors associated with this fit. With a UC content of about 1 wt%, these measurements are in agreement with elementary analyses on C concentrations, which were evaluated to about 500 µg g^{-1}.

4.2. Average coating thicknesses measured by HE-XRD

In the case of oxidized U–7Mo particles, equations (1) and (2) provided in §2 become

$$e = \left(\frac{3V_{\rm Core}}{4\pi}\right)^{1/3}\left[-1+\left(\frac{X_{\rm UO_2}}{X_{\rm UMo}+X_{\rm UC}}+1\right)^{1/3}\right]. \qquad (6)$$

The iterative process (see §2.1) was applied for the four different particles using theoretical densities (17.5, 13.6 and 11.0 g cm^{-3} for γ-U–7Mo, UC and UO_2, respectively) and the particle diameters reported in Table 1.

The obtained average thicknesses are given in Table 1. Errors related to these values are also indicated. They take into account two types of uncertainties: those associated with Rietveld refinement, which dominate, and those related to particle size/shape analysis. Larger errors for Particle_1 are

Table 2
Weight fractions and lattice constants obtained by Rietveld refinement of the XRD pattern on three powder samples and four single particles.

		Weight fraction of each crystallographic phase (wt%)					Lattice constants (a_0, Å)	
Sample	X-ray beam energy for HE-XRD (keV)	γ-U–Mo-a	γ-U–Mo-b	UC	Core	UO_2	γ-U–Mo-a	γ-U–Mo-b
Powder_A	90	42.0 (5)	49.5 (5)	1.9 (2)	93 (2)	6.6 (2)	3.433	3.439
Powder_B	90	42.0 (4)	48.0 (5)	0.7 (1)	91 (1)	9.3 (2)	3.433	3.439
Powder_C	90	34.3 (7)	60.0 (9)	0.5 (1)	95 (2)	5.3 (4)	3.433	3.439
Particle_1	60	82.5 (17)	9.1 (7)	0.8 (8)	92 (4)	7.6 (13)	3.429	3.440
Particle_2	90	51.8 (11)	41.3 (11)	0.7 (4)	94 (4)	6.0 (5)	3.429	3.440
Particle_3	90	55.4 (7)	40.4 (6)	1.0 (2)	97 (2)	4.3 (3)	3.429	3.440
Particle_4	90	58.2 (9)	36.9 (8)	1.0 (2)	96 (2)	4.0 (4)	3.429	3.440

Table 3
Agreement factors associated with the Rietveld refinement of the XRD pattern measured on three powder samples and four single particles.

Sample	R_p	R_{wp}	χ^2
Powder_A	9.3	8.5	6.4
Powder_B	7.5	7.3	8.1
Powder_C	10.6	7.4	8.1
Particle_1	11.9	6.7	9.0
Particle_2	10.3	9.0	7.5
Particle_3	9.0	7.8	7.3
Particle_4	8.7	7.6	8.5

due to the lower signal-to-noise ratio of the X-ray pattern measured on this small particle.

Whatever the particle diameter, the outer-shell thickness is evaluated as 0.9 (1) µm.

4.3. Coating imaging and average coating thickness measurement by nano-CT

To determine the outer oxide shell thickness, common synchrotron-based microtomography experiments with a spatial resolution of typically 1 µm do not provide the required level of detail. Such a measurement has been performed on Particle_1 on ID19 (ESRF) at 17 keV. The presence of an oxide outer shell was difficult to attest both because of its small thickness compared to the detector's point-spread function and because of strong diffraction of the X-ray light at interfaces within the sample. This last effect introduces a blurring of the outer surface of the U–Mo core and it becomes difficult to identify the oxide shell.

Tomographic investigations with a resolution in the deep sub-micrometre range (nano-CT) are suitable to depict the coating features. They were performed in absorption mode on ID22NI (see §3.3.3), and the in-house software *PyHST* was used for reconstructions (Banhart, 2008). Fig. 4 shows three reconstructions relating to three different *xy* planes in the same oxide particle (Particle_5). It appears that this particle exhibits three main characteristics. Firstly, an oxide shell is systematically present around a U–Mo core. Secondly, this outer oxide shell shows a very irregular thickness around the core. Finally, porosities with micrometre size may be located at the interface between the U–7Mo core and the shell. The last two results could not be shown by SEM observations of particle sections obtained by mechanical (destructive) polishing (Iltis, 2009). To conclude on the presence of porosities, it is likely that their presence in the as-fabricated powder explains the cracks shown after the hot-rolling step (Iltis, 2009).

Nano-CT measurements on Particle_5 and Particle_6 were performed at nine z positions along the rotation axis. They enabled the calculation of an average thickness for the outer shell of these particles. A four-step methodology was followed. Firstly, an appropriate threshold was defined in the *xy* slice so as to only display the outer shell. Secondly, a polar transformation for 360 equally distributed positions along this shell was calculated (Donnelly & Mothe, 2007). Thirdly, each line of this last image was analysed, thus providing 360 measurements per slice of the outer oxide shell. Finally, because of the spherical shape of the UMo particles, only the outer shell thickness measured in the equatorial plane represents the real shell thickness. For slices collected in a non-equatorial plane a correction has to be applied: the thickness provided directly by image analysis is only apparent. This feature can also be seen in Fig. 4, which shows the evolution of both apparent particle diameter and outer-shell thickness for three different nano-CT acquisitions along the rotation axis. To sum up, the real average thicknesses of the protective shell in Particle_5 and Particle_6 are gathered in Table 1. They are 0.79 (7) and 0.84 (7) µm, respectively.

5. U–7Mo powder case

5.1. Analytical expressions for the outer-shell thickness $e(V_{ratio})$

In §2.2 a complex equation relating the outer-shell thickness e, V_{ratio} (defined in §2.2) and $f_V(D)$ (the sample granulometry) was obtained. To provide for each powder sample an analytical formula of $V_{ratio}(e)$, the same granulometry was considered for each sample (see §3.2), but integrals were calculated over different ranges ([0; ∞], [0; 45 µm] and [45 µm; ∞] for Powder_A to Powder_C, respectively; see §3.1). The obtained expressions for $V_{ratio}(e)$ are

$$V_{ratio} = e(10.9587 - 0.42456e + 0.00580916e^2) \times 10^{-2} \quad (7)$$

for Powder_A,

$$V_{ratio} = e(15.4709 - 0.812505e + 0.014547e^2) \times 10^{-2} \quad (8)$$

for Powder_B and

$$V_{ratio} = e(10.1051 - 0.348396e + 0.00409368e^2) \times 10^{-2} \quad (9)$$

for Powder_C.

Interpolation of the $e(V_{ratio})$ curves with a second-order polynomial results in

$$e = 0.0004V_{ratio}^2 + 0.0902V_{ratio} + 0.0013 \quad (10)$$

for Powder_A,

$$e = 0.0003V_{ratio}^2 + 0.0629V_{ratio} + 0.0025 \quad (11)$$

for Powder_B and

$$e = 0.0004V_{ratio}^2 + 0.0979V_{ratio} + 0.001 \quad (12)$$

for Powder_C.

5.2. Coating thicknesses

For the three oxidized U–Mo powder samples, Fig. 5 shows the measured and calculated HE-XRD patterns, while Table 2 gathers the determined weight fraction associated with each crystalline phase.

From both equations (10)–(12) and the results of the HE-XRD study, the average protective shell thickness has been calculated for each powder sample. The obtained values are reported in Table 1. Indicated errors only take into account Rietveld refinement uncertainties.

The study of these samples clearly demonstrates that this average thickness does not strongly depend on the particle

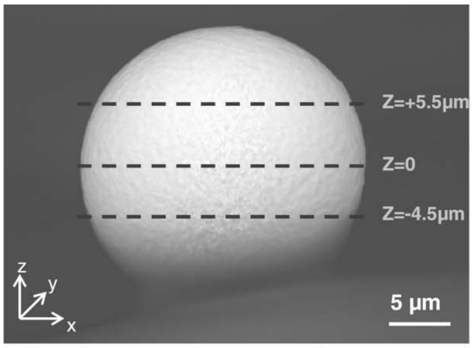

(a)

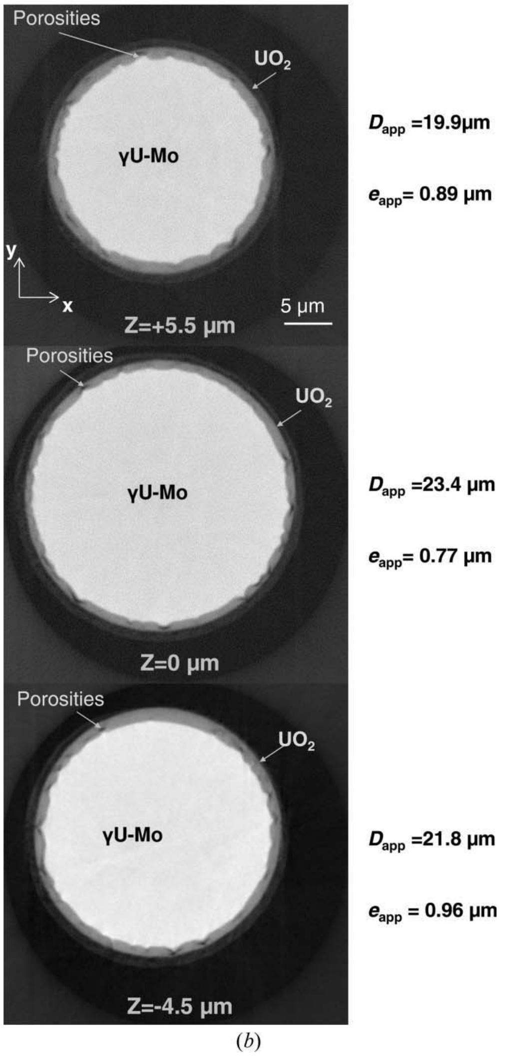

(b)

Figure 4
Three reconstructed *xy* slices (*b*) resulting from a nano-CT experiment performed on Particle_5 (*a*). D_{app} and e_{app} denote the apparent particle diameter and outer-shell thickness, respectively.

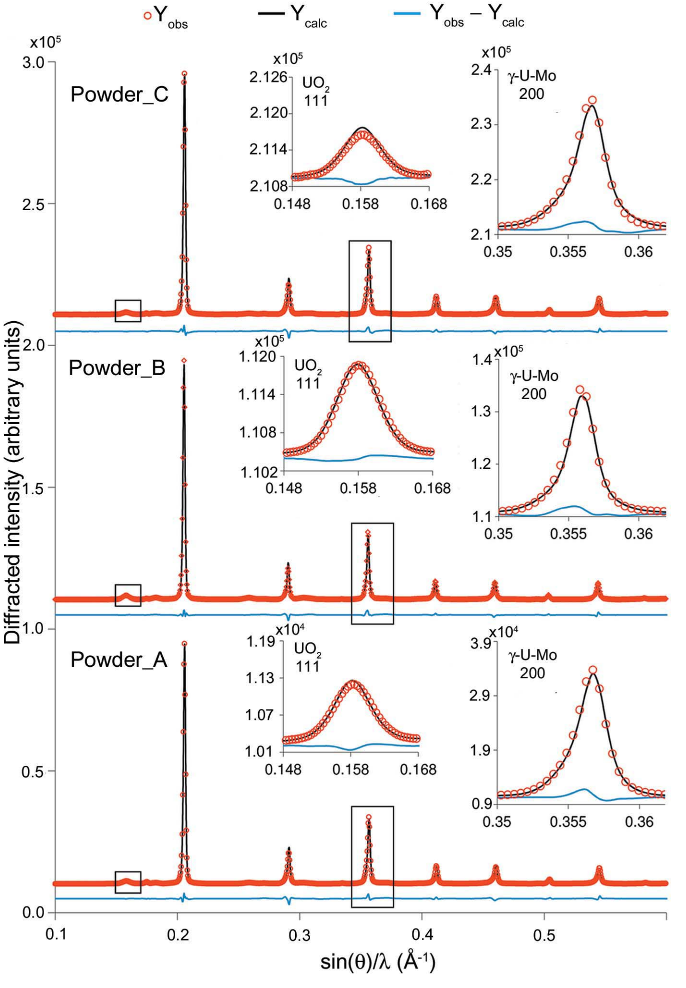

Figure 5
Measured and calculated high-energy X-ray diffraction patterns for the three U–7Mo oxidized powders (Powder_A, Powder_B and Powder_C). For each pattern insets show the asymmetry of the 220 γ-U–Mo Bragg line and the intensity of the 111 UO_2 Bragg line.

size: assuming a dense 100% oxide outer shell, the average thickness can be evaluated as 1.0 (1) μm.

6. Discussion

6.1. Comparison between the results provided by HE-XRD and nano-CT

Nano-CT at 17 keV and XRD at 87 keV lead to results in full agreement if one considers the errors associated with the measured values [1.0 (1) μm].

Nano-CT measurements on a larger number of U–Mo particles would be fruitful, especially for characterizing particles with larger diameter: this would, however, require the use of beams of the same size with a much higher energy (40–60 keV). These are not available for the moment on ID22NI. Nano-CT provides new information that is lost in the average diffraction measurements: the shell thickness is very irregular and micrometre-size porosities are located at the core–shell boundary.

As mentioned previously, the average outer-shell thickness derived from HE-XRD measurements depends on the density of the UO_2 phase in the shell. Calculations were first performed assuming a 100% density of UO_2. However, another outcome of these nano-CT measurements is the possibility to determine, through the reconstructed linear attenuation coefficient, the density of both the core and the outer shell. These values are very accurate for the U–Mo core but less precise for the oxide shell: the obtained values are 16.3 (7) g cm^{-3} (*i.e.* 93% of the γ-U–7Mo single-crystal theoretical density) and 9.5 (9) g cm^{-3} (*i.e.* 87% of the UO_2 single-crystal theoretical density), respectively. Using these quantities, the average outer thicknesses have been reevaluated for the diffraction data. These values are indicated in Table 1 and remain very close to those determined under the 100% density assumption.

Finally it should be noted that the obtained thicknesses for the UO_2 shell are in good agreement with those derived from SEM observations. This is an additional argument demonstrating the robustness of the developed methodology.

6.2. Limits of the method

Three limits associated with this methodology based on macroscopic HE-XRD can be found.

The first is linked to the assumed spherical shape of the particles, although it is clear that at least the largest exhibit an ellipsoidal shape. If this assumption is shown to be relevant, it is believed that, for U–Mo powders exhibiting a larger granulometry, the model presented here should take into account these nonspherical shapes.

The second is due to the presence of unidentified impurities in the U–Mo core. Even if the sum of these is very probably below 1 wt%, the presence of such phases affects the quality of the refinement and explains the large standard deviations obtained for the UO_2 weight fractions. New efforts to identify such impurities have to be undertaken.

Finally, all the phases present in the analysed particles have to be crystalline. More generally, the limits of this methodology are also those generally associated with powder diffraction (Hill & Howard, 1987; Madsen & Scarlett, 2008).

7. Conclusion

A methodology has been developed to determine the average outer-shell thickness of highly absorbing particles using a single macroscopic HE-XRD measurement on a large number of such particles (powder samples) and their characteristics in terms of granulometry. A good quantitative agreement was found between these macroscopic measurements and those performed on single particles by XRD or nano-CT. This demonstrates the relevance and reliability of this approach. However, it is clear that full-field CT measurements resulting in volume images of complete U–7Mo particles with large diameters would have been particularly helpful to investigate with even more detail the potential and limitations of this method.

As far as the low-enriched U–Mo nuclear fuel development is concerned, this work should enable the measurement of the thickness of coatings obtained either (i) by physical vapour deposition or chemical vapour deposition techniques on powders or (ii) by diffusion of elements (such as Si) added to the matrix during fuel plate manufacture. In this last case, the crystallographic composition of these layers (SiRDL) has already been determined using transmission electron microscopy (Yao *et al.*, 2011) and XRD (Palancher *et al.*, 2012). Therefore, measurements of SiRDL thickness should soon be feasible.

More generally, this approach should be suitable for application to any kind of highly absorbent crystalline core–shell systems.

APPENDIX *A*
Comment on the trace phase found in the particle core

In the core of U–Mo particles a trace phase has been detected. Its most intense peaks are found at 2.78, 1.84, 1.62 and 1.35 Å (d_{hkl} values). Using a tetragonal crystal system and refined lattice constants ($a = b$= 4.848, c = 3.449 Å), these Bragg lines could be indexed to 101, 211, 300 and 102, and 212 and 320. Such a phase has already been found in U–Mo samples, *i.e.* U–Mo ingots (Tangri & Williams, 1961) and U–10Mo atomized powders (Seong *et al.*, 2000). In these studies, this phase is referred to as $U_{22}Mo_3$ and U_3Mo, respectively. However, the reported crystal structure (Seong *et al.*, 2000) is not fully consistent with the measured intensity for some Bragg lines (*i.e.* 100, 001, 110 . . .). Because of the low weight fraction of this phase and because of the overlap between the Bragg lines of this trace phase and those of γ-U–Mo, its crystal structure could not be refined.

Finally, based on our study, it remains difficult to definitely assess whether this trace phase is related to an ordered metastable phase γ-U-Mo (also written γ^0 in the literature) or to an impurity.

The authors are grateful to X. Iltis (CEA, DEC) for providing the U–Mo powder granulometry measurements, and C. Tanguy (CEA, DEC) is warmly thanked for her experimental and technical contributions to this work. Professor W. Petry (TUM/FRM II) and F. Charollais (CEA, DEC) are acknowledged for their valuable advice. A reviewer is also thanked for constructive comments and suggestions.

References

Banhart, J. (2008). *Advanced Tomographic Methods in Materials Research and Engineering.* Oxford University Press.

Bonnin, A., Palancher, H., Honkimäki, V., Tucoulou, R., Calzavara, Y., Colin, C. V., Bérar, J.-F., Boudet, N., Rouquette, H., Raynal, J., Valot, C. & Rodriguez-Carvajal, J. (2011). *Z. Kristallogr. Proc. 1*, pp. 29–34.

Bleuet, P., Cloetens, C., Gergaud, P., Mariolle, D., Chevalier, N., Tucoulou, R., Susini, J. & Chabil, A. (2009). *Rev. Sci. Instrum.* **80**, 056101.

Charollais, F., Lemoine, P., Calzavara, Y., Guyon, H., Koonen, E., Van den Berghe, S., Stepnik, B., Jarousse, C. & Geslin, D. (2011). Proceedings of RERTR2011, 22–26 October 2011, Santiago, Chile.

Coster, M. & Chermant, J. L. (1989). *Précis d'Analyse d'Images*, 22nd ed. Paris: Presses du CNRS.

Donnelly, E. & Mothe, F. (2007). *Polar Transformer*, http://rsbweb.nih.gov/ij/plugins/polar-transformer.html.

Garrido, F., Hannon, A. C., Ibberson, R. M., Nowicki, L. & Willis, B. T. M. (2006). *Inorg. Chem.* **45**, 8408–8413.

Hammersley, H. (1999). *The FIT2D Home Page*, http://www.esrf.eu/computing/scientific/FIT2D/.

Hill, R. J. & Howard, C. J. (1987). *J. Appl. Cryst.* **20**, 467–474.

Iltis, X. (2009). Internal Report NT LCU 09-020. CEA, Cadarache, France.

Iltis, X., Charollais, F., Anselmet, M. C., Lemoine, P., Leenaers, A., Van den Berghe, S., Koonen, E., Jarousse, C., Geslin, D., Frery, F. & Guyon, H. (2010). Proceedings of RERTR 2010, 10–14 October 2010, Lisbon, Portugal.

Jarousse, C., Bourdat, G., Ripert, M., Boulcourt, P. & Lemoine, P. (2008). Proceedings of RRFM 2008, 2–5 March 2008, Hamburg, Germany.

Keiser, D. D. Jr, Jue, C. R., Woolstenhulme, N. & Ewh, A. (2011). *J. Nucl. Mater.* **419**, 226–234.

Keiser, D. D. Jr, Robinson, A. B., Jue, J.-F., Medvedev, P., Wachs, D. M. & Finlay, M. R. (2009). *J. Nucl. Mater.* **393**, 311–320.

Leenaers, A., Van den Berghe, S., Koonen, E., Jarousse, C., Huet, F., Trotabas, M., Boyard, M., Guillot, S., Sannen, L. & Verwerft, M. (2004). *J. Nucl. Mater.* **335**, 39–47.

Madsen, I. C. & Scarlett, N. V. Y. (2008). *Powder Diffraction, Theory and Practice*, edited by R. E. Dinnebier & S. J. L. Billinge, ch. 11. Cambridge: RSC Publishing.

Martin, P., Ripert, M., Petit, T., Reich, T., Hennig, C., D'Acapito, F., Hazemann, J. L. & Proux, O. (2003). *J. Nucl. Mater.* **312**, 103–110.

Martínez-Criado, G. *et al.* (2012). *J. Synchrotron Rad.* **19**, 10–18.

Palancher, H., Bonnin, A., Honkimäki, V., Buslaps, T., Grasse, M., Stepnick, B. & Zweifel, T. (2012). *J. Alloys Compd.* **527**, 53–65.

Palancher, H., Tucoulou, R., Bleuet, P., Bonnin, A., Welcomme, E. & Cloetens, P. (2011). *J. Appl. Cryst.* **44**, 1111–1119.

Park, J. M., Ryu, H. J., Kim, K. H., Lee, D. B., Lee, Y. S., Lee, J. S., Seong, B. S., Kim, C. K. & Cornen, M. (2010). *J. Nucl. Mater.* **397**, 27–30.

Ripert, M., Marelle, V., Iltis, X., Palancher, H., Valot, Ch., Charollais, F., Anselmet, M.-C., Tiratay, X., Lemoine, P., Van den Berghe, S., Leenaers, A. & Jarousse, C. (2011). Proceedings of RRFM 2011, 20–24 March 2011, Rome, Italy.

Rodriguez-Carvajal, J. (1990). *FULLPROF.* Version 4.4. Institut Laue–Langevin, Grenoble, France, http://www.ill.eu/sites/fullprof.

Ryu, H. J., Park, J. S., Park, J. M. & Kim, C. K. (2011). *Nucl. Eng. Technol.* **43**, 159–166.

Seong, B.-S., Lee, C. H., Lee, J.-S., Shim, H.-S., Lee, J.-S., Kim, K. H., Kim, C. K. & Em, V. (2000). *J. Nucl. Mater.* **277**, 274–279.

Tangri, K. & Williams, G. I. (1961). *J. Nucl. Mater.* **4**, 226–233.

Van den Berghe, S., Leenaers, A., Koonen, E. & Sannen, L. (2010). *Adv. Sci. Technol.* **73**, 78–90.

Yao, B., Perez, E., Keiser, D. D. Jr, Jue, J.-F., Clark, C. R., Woolstenhulme, N. & Sohn, Y. (2011). *J. Alloys Compd.* **509**, 9487–9496.